

Journal of Biomedical Optics

SPIDigitalLibrary.org/jbo

Digital optical tomography system for dynamic breast imaging

Molly L. Flexman
Michael A. Khalil
Rabah Al Abdi
Hyun K. Kim
Christopher J. Fong
Elise Desperito
Dawn L. Hershman
Randall L. Barbour
Andreas H. Hielscher

Digital optical tomography system for dynamic breast imaging

Molly L. Flexman,^a Michael A. Khalil,^a Rabah Al Abdi,^b Hyun K. Kim,^a Christopher J. Fong,^a Elise Desperito,^c Dawn L. Hershman,^d Randall L. Barbour,^{b,e} and Andreas H. Hielscher^{a,c,f}

^aColumbia University, Department of Biomedical Engineering, 351 Engineering Terrace, 1210 Amsterdam Avenue, New York, New York 10027

^bState University of New York – Downstate Medical Center, Department of Pathology, Box 25, 450 Clarkson Avenue, Brooklyn, New York 11203

^cColumbia University Medical Center, Department of Radiology, 630 West 168th Street, Box 28, New York, New York 10032

^dColumbia University Medical Center, Department of Medicine – Oncology, Irving Pavilion, 161 Fort Washington Avenue, New York, New York 10032

^eNIRx Medical Technologies LLC, Glen Head, New York 11545

^fColumbia University, Department of Electrical Engineering, 1300 S.W. Mudd, 500 West 120th Street, New York, New York 10027

Abstract. Diffuse optical tomography has shown promising results as a tool for breast cancer screening and monitoring response to chemotherapy. Dynamic imaging of the transient response of the breast to an external stimulus, such as pressure or a respiratory maneuver, can provide additional information that can be used to detect tumors. We present a new digital continuous-wave optical tomography system designed to simultaneously image both breasts at fast frame rates and with a large number of sources and detectors. The system uses a master-slave digital signal processor-based detection architecture to achieve a dynamic range of 160 dB and a frame rate of 1.7 Hz with 32 sources, 64 detectors, and 4 wavelengths per breast. Included is a preliminary study of one healthy patient and two breast cancer patients showing the ability to identify an invasive carcinoma based on the hemodynamic response to a breath hold. © 2011 Society of Photo-Optical Instrumentation Engineers (SPIE). [DOI: 10.1117/1.3599955]

Keywords: diffuse optical tomography; dynamic imaging; digital signal processor; digital detection; breast cancer; continuous wave; optical instrumentation; optical mammography.

Paper 11155R received Mar. 28, 2011; revised manuscript received May 19, 2011; accepted for publication May 23, 2011; published online Jul. 13, 2011.

1 Introduction

Breast cancer affects approximately one in eight women in the United States and the incidence of breast cancer throughout the world is increasing.¹ Breast cancer currently accounts for 28% of all new cancers diagnosed in women and causes almost 40,000 deaths each year.² The most commonly applied modality for breast cancer screening is x-ray mammography. However, its use of ionizing radiation limits the frequency with which this modality can be employed. Furthermore, mammography has shown to be less reliable for young women, it causes patient discomfort, and its high false positive rate means that after 10 mammograms as many as one in two women will have had at least one false positive.^{3,4} As an alternative to x-ray mammography, magnetic resonance imaging (MRI) has proven to be a powerful tool in monitoring high-risk women; but its high cost and variable specificity hinders its use as a screening modality.³ Ultrasound imaging is commonly used as a second-line diagnostic tool to differentiate masses detected by x-ray mammography; but operator variability and low specificity make it unsuitable for front-line screening.³

Over the last decade, diffuse optical tomography (DOT) has emerged as a novel biomedical imaging modality that may be able to address some of the shortcomings of other breast imaging

modalities.^{5,6} DOT uses low-intensity light in the near-infrared to infrared wavelength range to probe and characterize breast tissue. The use of nonionizing radiation and low cost of this imaging modality make it potentially ideal for breast cancer screening. DOT derives contrast from physiological changes in tissue that can be used to detect and characterize cancerous lesions. For example, growing tumors require increased vascularization to continue to receive adequate blood supply and the vasculature formed by tumors tends to be much more chaotic and leak more than vasculature in normal tissue.⁷ These physiological changes result in measureable changes in the behavior of light passing through the tumor tissue as compared to the surrounding tissue. By using multiple wavelengths of light it is possible to extract the concentrations of the primary light absorbers in the breast including oxygenated and deoxygenated hemoglobin, lipid, and water. Furthermore, light is also sensitive to scattering changes in tissue. Researchers have shown that differences in the scattering properties of tissue, due to cellular changes such as enlarged and denser nuclei, can be used to detect breast cancer.^{8,9} Specifically, increases in scattering power and scattering amplitude can differentiate certain types of cancer from healthy tissue.¹⁰

Many research groups have made significant advances in the field of DOT breast imaging, employing a variety of designs for instrumentation.^{11–18} Time-domain (TD) systems inject a short

Address all correspondence to: Molly Flexman, Columbia University, Biomedical Engineering, 351 Engineering Terrace, 1210 Amsterdam Avenue, New York, New York 10027; Tel: 212 342 0086; E-mail: mlf2129@columbia.edu.

light pulse (full-width-half-maximum typically less than 0.1 ns) into the breast and measure the time-dependent transmitted intensities. These systems provide a wealth of information about the optical properties of the tissue, however, data acquisition typically takes three to five minutes and the systems are comparably expensive. Taroni et al. have shown an 80% sensitivity in detecting breast lesions with a five to seven wavelength TD system in a retrospective study of 194 patients.¹² In particular, they showed that while strong absorption of blood at the short wavelengths is a hallmark of tumors, it is low scattering across wavelengths, and low absorption around the lipid peak (905 to 916 nm) that allows for the differentiation of cysts. Rinneberg et al. also showed sensitivity and specificity between 80 and 85% for tumor detection in a study of 154 patients using a 2-wavelength TD system.¹³

Another class of systems uses amplitude-modulated light instead of a short light pulse to probe the breast tissue. These frequency-domain (FD) systems operate at one or several source-modulation frequencies and gather data on both the amplitude and phase of the light that passes through the tissue. FD instrumentation is typically less expensive and allows for faster data acquisition than TD systems. Using this technology, Choe et al. showed the ability to differentiate between benign and malignant tumors in 47 subjects with a sensitivity and specificity of 98 and 90%.¹⁵ Analyzing data from 60 healthy patients, Srinivasan et al. conducted one of the most comprehensive studies on the properties of normal breast tissue using a six-wavelength FD system,¹⁶ and Wang et al. have extended that work to show promising results in small populations of breast cancer patients.¹⁹

The third class of DOT systems does not rely on a time-varying light source and instead injects a steady-state beam of light into the breast. Known as continuous-wave (CW) systems, the instrumentation measures solely the change in the amplitude of the light as it passes through the breast, which results in simpler, more affordable technology. While no phase information is provided, this approach allows for faster data acquisition than in FD or TD systems, which makes it possible to study time-varying dynamic signals. Several groups have made successful use of CW instrumentation for breast cancer detection including Liang et al. who showed sensitivity and specificity of 82 and 71% in 33 patients¹⁷ and van de Ven et al. who showed detection rates of 60 to 80% in 17 patients.¹⁸

In addition to these three classes of optical tomography imaging systems (TD, FD, and CW), a number of promising hybrid systems have been developed that combine DOT with other imaging modalities such as x-ray mammography,²⁰ ultrasound,^{21,22} and MRI.^{23,24}

Regardless of the type of instrumentation, all DOT systems rely on endogenous contrast generated by the physiology of tissue, either in steady state or after perturbing the state of the physiology in order to generate a transient response to differentiate between healthy and cancerous tissue. Due to excess endothelial cells and abnormal perivascular cells, tumor vasculature is disorganized and hyper-permeable.²⁵ The leakiness of the vessels makes them unable to maintain a pressure gradient between the vessels and the interstitial space and also impairs the flow of fluid and molecules. In addition, tumor cells consume large amounts of oxygen which, coupled with poor oxygen delivery, leads to tumor hypoxia. Overall, these changes affect the hemodynamic

response of the cancerous tissue, providing additional information about the tissue that can be used for diagnosis. Some common sources of dynamic contrast used to evoke a hemodynamic response include a respiratory maneuver,²⁶ the application of pressure to the breast,^{27,28} the respiration of carbogen,²⁹ and the injection of indocyanine green.³⁰⁻³²

In exploring dynamic changes it is important to have adequate temporal resolution to capture the transient responses. In addition, a large number of source and detector positions are required to cover the breast for good 3D spatial resolution.³³ Further, simultaneously imaging both breasts allows for the contra-lateral breast to serve as a reference that is under the same external stimulus as the tumor-bearing breast. To accomplish these imaging goals, it is essential to have a system that can acquire a large amount of data at fast imaging speeds. In addition, the large geometries involved in breast optical tomography necessitate a large dynamic range to capture the varying amplitudes of reflected and transmitted light. Existing systems used in dynamic imaging studies are limited in three-dimensional spatial resolution, temporal resolution, or dynamic range and most existing systems only image one breast at a time.

Here, we present a novel CW optical tomographic breast imaging system designed for dynamic optical breast imaging. To overcome the inherent difficulty in obtaining high frame rates while collecting large amounts of data, we expanded upon the concept of digital-based detection previously introduced by our group.³⁴ This new system extends the digital detection concept by using multiple digital signal processing (DSP) chips arranged in a master-slave setup to maximize the processing throughput, reduce noise, and provide a system design that can be scaled to accommodate a variable number of detectors and wavelengths. The system can simultaneously image both breasts at 1.7 Hz using four wavelengths, 64 sources, and 128 detectors with a large dynamic range (10^8). In three case studies involving two breast cancer patients and one healthy volunteer, we illustrate a clinical application of the system in studying the breast hemodynamic response.

2 Instrument Design

The new digital optical tomography system is composed of a light input unit for generating the laser light, a detection unit for measuring and quantifying the light, and a user interface unit involving a host computer to allow the operator to control and view the results of the imaging. An overview of the system is shown in Fig. 1.

2.1 Light Input Unit

The input unit is responsible for generating the light with which the target will be illuminated. The system uses four wavelengths of near-infrared light at 765, 808, 827, and 905 nm generated by continuous-wave high power laser diodes (HPD-1010-HHLF-TEC, High Power Devices, Inc.). Each laser diode is controlled by a laser driver controller (ITC110, Thorlabs Inc.) and modulated with an input current at either 5 kHz (765 and 808 nm) or 7 kHz (827 and 905 nm). Modulating the laser light intensity allows for simultaneous illumination of the target with multiple wavelengths as well as the rejection of ambient light. The four wavelengths are passed through two wave-division

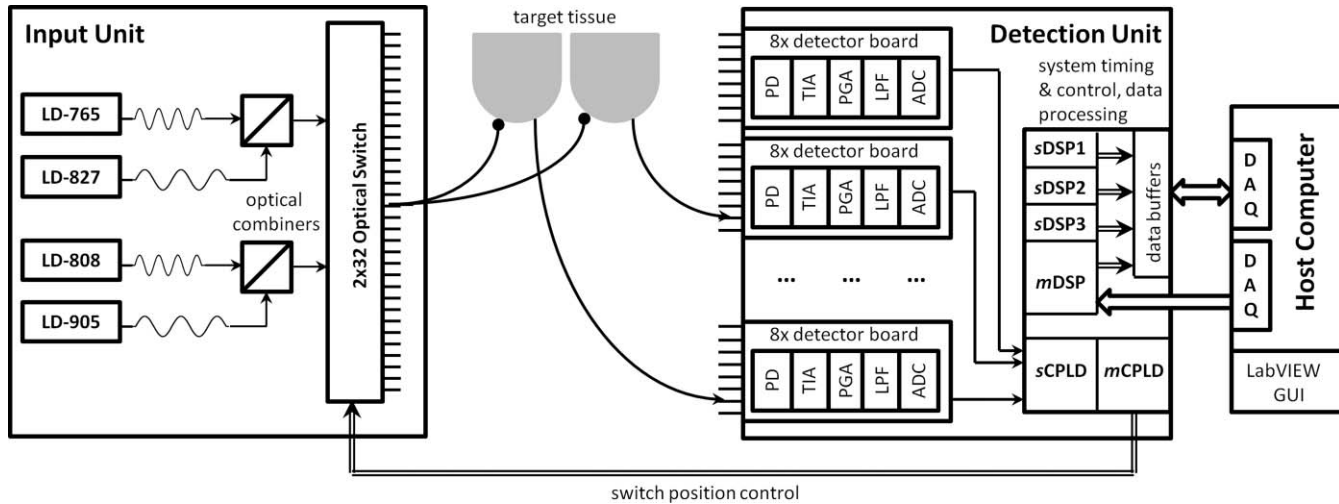


Fig. 1 Diagram outlining the three main components of the system: the light input unit, the detection unit, and the host computer.

multiplexers (Oz Optics Ltd.) to create two separate streams of light: one stream that combines 765 nm modulated at 5 kHz and 827 nm modulated at 7 kHz, and one stream that combines 808 nm modulated at 5 kHz and 905 nm modulated at 7 kHz. Due to the fact that each stream must be detected with the same hardware, the same amount of gain must be applied to all wavelengths of the stream. In cases where the attenuation through the tissue is significantly different at the various wavelengths, it can be difficult to find one gain setting to accommodate all four wavelengths. Thus, our design uses two streams of light with two wavelengths in each stream that tend to experience similar attenuation. Each modulation frequency is generated by a direct digital synthesis (DDS) chip (AD9854, Analog Devices Inc.) and passed through a series of filters as well as offset and amplitude adjustment stages prior to being input to the laser driver controller. The output frequency of the DDS chip is controlled by a programmable microcontroller (AT89S8253, Atmel).

The two light streams are passed into a 2×32 optomechanical switch (Sercalo Rack System Solutions, RS-FSPA $2 \times 1 \times 32$ -62FCPC). The switch begins by illuminating the target at one source position with the first wavelength set (765 and 827 nm) and then the second wavelength set (808 and 905 nm) before moving onto the next source position. It continues this source switching until all programmed source positions (up to 32 per breast) have illuminated the target. The switching is customizable so that the system can run with only two wavelengths twice as quickly since it does not need to repeat the measurements at each source position a second time for the additional wavelength set. The optical switch takes less than 7 ms to settle when switching between positions.

Multimode 62/125 optical fibers leave the switch and then bifurcate to simultaneously illuminate both the left and right breast with 4-mm-diameter tips. The fibers are brought into contact with the breast using a hand-like measuring apparatus developed by NIRx Medical Technologies, shown in Fig. 2. In the measuring apparatus, 16 sources and 16 detectors are arranged in a flat geometry beneath the breast, while the other 16 sources and 16 detectors are brought into contact with the top of the breast with eight adjustable fingers, each one holding four fibers. All sources are co-localized with detector fibers, giving

each breast a total of 64 detectors and 32 sources. The setup is designed to minimize patient discomfort by imaging without compression and with the patient in a comfortable seated or standing position.

2.2 Light Detection Unit

The light detection unit is the key component of the system as its design allows for the fast collection and processing of large amounts of data. An overview of the interactions between the various boards and chips that make up the detection unit is presented in Fig. 3. The detection unit starts with analog circuitry to amplify and filter the signal prior to quantization with an analog-to-digital converter (ADC). The ADC interacts with a complex programmable logic device (CPLD) and DSP chip that



Fig. 2 Photograph of the interface used to bring the optical fibers in contact with the breast. Articulating fingers bring 32 fibers into contact with the top portion of the breast, while 32 fibers arranged in a flat geometry make contact with the bottom portion of the breast. Half of the fibers are both sources and detectors while the other half are dedicated detectors.

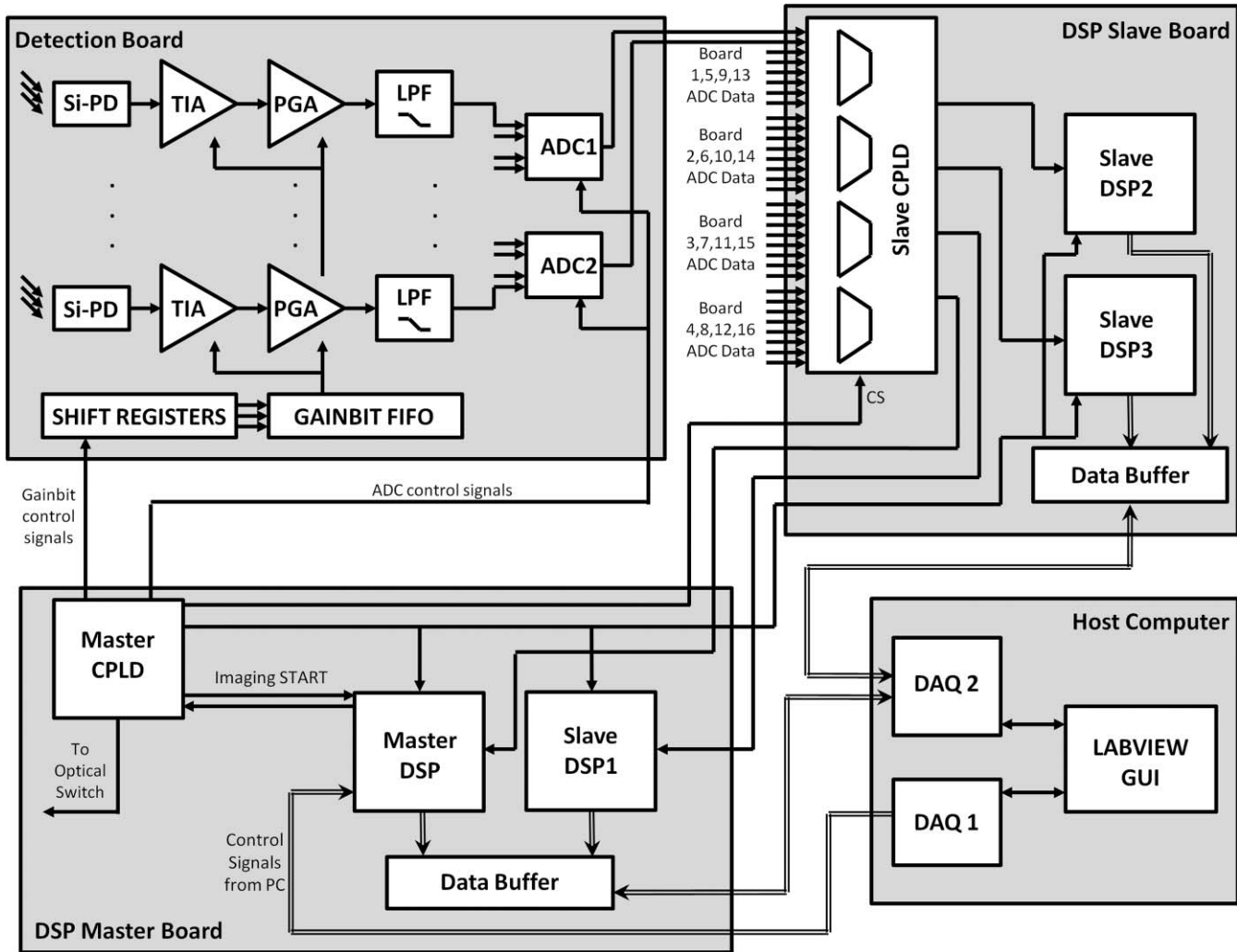


Fig. 3 Overview of the detection circuitry and logic showing the interaction between the DSP master board, DSP slave board, detection boards, and host computer.

work to acquire the signal, demodulate the signal to extract the amplitude, and pass the amplitude onto the host computer via data acquisition cards. The DSP and CPLD chips also coordinate the timing of the system and keep the various components synchronized while optimizing the system performance. Power to the detection unit is provided by a compact peripheral component interconnect (PCI) power supply (Chroma cPWR-59401) that provides voltage rails at +5, +3.3, +12, and -12 V.

2.2.1 Analog detection electronics

The analog portion of the detection unit involves converting the detected photons into an electronic signal and then conditioning that signal in preparation for digitization. The first stage of the analog electronics consists of a silicon photodiode (Si-PD: Hamamatsu S1337-33BR) that converts the incident photons into a current that is then amplified and output as a voltage using a trans-impedance amplifier (TIA). The trans-impedance amplifier uses a bandwidth extension technique to enable high gain and sufficient bandwidth for the 5 and 7 kHz signals that must be amplified.³⁵ Following the TIA, a passive RC high-pass

filter removes the DC component of the signal. From there, the signal passes through a second gain stage referred to as the programmable gain amplifier (PGA) that provides additional amplification, but no additional signal-to-noise ratio (SNR). The PGA is primarily responsible for bringing the signal into a suitable range for detection with the ADC.

To control the resistor values across the TIA and the PGA gain stages, three bits are used to encode a range of gain settings. The resistor values for the TIA range from 10 k Ω to 100 M Ω and the PGA gain ranges from 1 to 100. The three gain bits control the resistor value for the TIA and PGA via a multiplexer and reed relays that are used to switch between the values. The available gain bits and their TIA and PGA gain are shown in Table 1. The gain bits can be manually controlled through the host computer user interface or through an automatic detection routine that will test and select the optimal settings. The optimal setting is determined as the best SNR without saturation. The host computer passes the gain bits to the DSP through a series of shift registers that daisy-chain through the detection boards. Once all of the gain bits have been chained through the boards, a signal transfers the gain bits into a first-in-first-out (FIFO)

Table 1 Description of the detection gain settings.

Gain setting	Overall gain (V/A)	TIA gain (V/A)	PGA gain (V/V)
1	10 k	10 k	1
2	100 k	10 k	10
3	1 M	10 k	100
4	10 M	10 M	1
5	100 M	10 M	10
6	1 G	10 M	100
7	10 G	100 M	100

buffer for storage on each detection board. During imaging, as the source position is changed, the new gain bit settings are read out locally from the FIFO thereby quickly modifying the resistor values across the TIA and PGA.

Following the TIA and PGA gain stages, the signal is filtered with an eighth-order Butterworth anti-aliasing filter that removes high-frequency components and whose primary purpose is to ensure that there are no frequencies present above the Nyquist frequency prior to digitization. The signal is sampled at 75 ksamples/s, which means that the Nyquist frequency is 37.5 kHz. As a result, we choose a cutoff frequency of 12.5 kHz and a Butterworth filter that has a flat passband for the 5 and 7 kHz signals, while also providing strong attenuation of any higher frequency noise at risk of aliasing into the passband. Furthermore, an operational amplifier offsets the signal so that it is centered around 2.5 V in order to take advantage of the full 0 to 5 V input range of the ADC.

Finally, the signal is brought into the digital domain using a four channel, 16-bit, successive approximation register ADC (AD7655, Analog Devices Inc.) that samples at a maximum rate of 1 Msamples/s. In our system, the ADC samples the data from each detector channel at 75 kHz. The ADC timing is synchronized with the rest of the digital electronics through the master CPLD and DSP.

2.2.2 Master-slave architecture

The major difference between the DSP-based system previously developed by our group for small animal and finger imaging³⁴ and this new breast imaging system is the realization of a master-slave architecture for expanding the data acquisition capabilities to multiple DSP chips as opposed to a single DSP chip. This design was necessitated by the increase in sources, detectors, and wavelengths required for breast imaging. The master DSP (*mDSP*) chip is the single DSP that coordinates the behavior of the system, including the other slave DSP (*sDSP*) chips. It handles all of the handshaking with the host computer and works with the master CPLD (*mCPLD*) to control the timing of the optical switch, gain bits, and acquisition of the signals from the ADCs. The *mDSP* relies heavily on the *mCPLD* to control the timing of all of the signals related to shifting and setting the gain bits, controlling the conversion and sampling from the

ADCs, and sending out the address signals to control the source position of the optical switch.

The *mDSP* and *mCPLD* work closely together to control the timing of the events in the system and to communicate with the other chips. The *mCPLD* is used to communicate the control logic to the detection boards, but the *mDSP* closely controls the *mCPLD* and is responsible for timing the 7 ms for the optical switch settling. The intricate way in which the *mDSP* and *mCPLD* work together to progress through the various states of setup and acquisition is shown in Table 2.

The *mDSP* also relies on a slave CPLD (*sCPLD*) whose job is to multiplex the incoming data from the 32 detector ADC chips (each responsible for digitizing four detector channels) and routing it to the DSP chips for processing. This multiplexing is controlled through a chip-select (CS) signal that keeps the CPLDs, ADCs, and DSPs in sync. Each DSP acquires two simultaneous serial streams of data through the A and B serial ports. We refer to one DSP as the master DSP (*mDSP*) because it is in charge of the system, while the other three DSP chips (*sDSP1*, *sDSP2*, *sDSP3*) are referred to as slave chips because they have no understanding of what is going on and can only respond to one signal (imaging start) that tells them to either acquire data or sit idly. The master-slave configuration helps simplify the control of the system and keeps the data acquisition for all DSP chips in unison. This configuration also allows for easy scaling of the system for a larger number of sources, wavelengths, or detectors, which is achieved either by reprogramming the existing DSPs or by adding additional slave DSP chips.

Each pair of DSP chips (*mDSP* & *sDSP1* and *sDSP2* & *sDSP3*) share an 8192×9 dual synchronous FIFO (IDT 72851) through which the data is sent back to the host computer. The DSP chips write to the FIFO, which modifies the “EMPTY” signal of the FIFO, thereby triggering a request to the host computer. The host computer then grants the request and triggers a read to the FIFO, which sends the data to a LabVIEW user interface. As a result, the FIFO is essentially a data buffer that is responsible for holding the data until the host computer is ready. The control signals from the user interface are passed to the detector hardware through a National Instruments Data Acquisition Card (NI PCI-6503) that is a 24 bit digital I/O interface. The data from the DSP chips is acquired by the host computer through a National Instruments Acquisition Card (NI PCI-6533) that provides 32 digital data lines that are individually configurable as input or output, grouped into four 8-bit ports. Each group of 8-bit ports is devoted to one DSP in order to handle the data transfer to the host computer.

2.2.3 Digital demodulation

Each DSP is responsible for demodulating the incoming data to extract the amplitude of the signal. The digital lock-in detection algorithm employed by this system was previously described in detail by Masciotti et al.³⁶ The key feature of the algorithm is that it uses a simple averaging filter to extract the amplitude of the signal, but requires a specific relationship between f_m , the frequency of the signal (7 and 5 kHz in this system), and N_s , the number of samples acquired, as shown in the following

Table 2 State by state description of the PC, *mCPLD*, and *mDSP* interaction.

State	Description
Standby	<i>mDSP</i> is idle waiting for a signal from the host computer. <i>mCPLD</i> is idle waiting for a signal from the <i>mDSP</i> .
System parameters	1. <i>mDSP</i> receives CMD:01 from the host computer telling it to go into the System Parameters state. 2. The host computer sends the number of sources, detectors, and wavelengths to the <i>mDSP</i> . 3. <i>mDSP</i> returns to Standby. * <i>mCPLD</i> remains in Standby.
Gain Bit	1. <i>mDSP</i> receives CMD:10 from the host computer telling it to go into the Gain Bit download state. 2. PC sends the gain bits for each source-detector pair. 3. <i>mDSP</i> tells the <i>mCPLD</i> to go into Gain Bit state. 4. <i>mDSP</i> sends the <i>mCPLD</i> the # of sources, detectors, wavelengths. 5. <i>mDSP</i> sends the gain bits through the <i>mCPLD</i> to the detection boards while the <i>mCPLD</i> sends out control signals to the Gain Bit Shift Registers and FIFOs. 6. <i>mDSP</i> and <i>mCPLD</i> return to Standby.
Imaging	1. <i>mDSP</i> receives CMD:11 from the host computer telling it to acquire one frame. 2. <i>mDSP</i> tells <i>mCPLD</i> to go into Imaging State. 3. <i>mCPLD</i> tells the optical switch to move to the next position. Updates the gain bits by reading from the detection board FIFOs. Waits for the TIMER signal from <i>mDSP</i> . 4. DSP counts to 7 ms and then signals TIMER to <i>mCPLD</i> . During that time, it also runs the lock-in detection and sends data from previous source back to the PC. 5. <i>mCPLD</i> acquires 150 samples from all detectors. 6. <i>mDSP</i> receives data from the ADC. Returns to step 3 until all sources and wavelength sets are acquired. 7. <i>mDSP</i> and <i>mCPLD</i> return to Standby.

equation:

$$f_m = \frac{kf_s}{N_s}, \quad 1 \leq k < \frac{N_s}{2}. \quad (1)$$

Performing the lock-in detection digitally using a DSP chip as opposed to using traditional analog circuitry not only reduces the amount of hardware required for demodulation, but also provides a more robust solution with better noise performance.^{37,38} Simply by reprogramming the DSP chip it is possible to adjust the lock-in frequency, filtering, and the number of detectors. In addition, DSP-based demodulation is less sensitive to analog component tolerances that can vary with temperature and age as well as between detector channels.³⁹

2.2.4 System timing

To obtain fast imaging speeds, it is important to have careful coordination between the various components of the system, while also accounting for the settling times of the electronics

and optical switch. There are many occasions where the system multi-tasks to optimize the imaging speed. The system timing is outlined in detail in Fig. 4.

The DSPs acquire 150 samples from each of the 128 detectors over a period of 2 ms so that each detector is effectively sampled at 75 ksamples/s. The chip select (CS) signal sequentially selects two ADCs per DSP at a time to pass the digitized samples onto that DSP. Each 16-bit ADC can digitize two channels at a time and passes them onto the DSP as one 32-bit packet. For example, *mDSP* first receives sample 1 from channels 1&3 of ADCs 1&2, followed by sample 1 from channels 1&3 of ADCs 3&4, followed by sample 1 from channels 1&3 of ADCs 5&6, and finally sample 1 from channels 1&3 of ADCs 7&8. It then proceeds to acquire sample 1 from channels 2&4 from each set of ADCs before moving onto the next sample. In parallel, *sDSP1*, *sDSP2*, and *sDSP3* are receiving data from ADCs 9 through 32. The *sCPLD* is responsible for coordinating the routing of the ADC data to the appropriate DSP in each cycle, as coordinated by the CS signal.

	Adjust Optical Switch and Update Gain Settings for:	Illuminate Sample With:	Convert Sample:	Send Data for ADC Channels:	mDSP	sDSP1	sDSP2	sDSP3	DSPs Demodulate & Send Data to PC for:		
7ms ↓ 2ms	SRC1, WL1&2										
		SRC1, WL1&2	Sample 1	Channel 1&3	ADC1&2	ADC9&10	ADC17&18	ADC25&26			
					ADC3&4	ADC11&12	ADC19&20	ADC27&28			
					ADC5&6	ADC13&14	ADC21&22	ADC29&30			
					ADC7&8	ADC15&16	ADC23&24	ADC31&32			
				Sample 1	Channel 2&4	ADC1&2	ADC9&10	ADC17&18		ADC25&26	
			ADC3&4			ADC11&12	ADC19&20	ADC27&28			
			ADC5&6			ADC13&14	ADC21&22	ADC29&30			
			ADC7&8			ADC15&16	ADC23&24	ADC31&32			
				Sample 2	Channel 1&3	ADC1&2	ADC9&10	ADC17&18		ADC25&26	
				
				Sample 150	Channel 2&4	ADC7&8	ADC15&16	ADC23&24		ADC31&32	
			SRC1, WL3&4								SRC1, WL1&2
				SRC1, WL3&4	Sample 1	Channel 1&3	ADC1&2	ADC9&10		ADC17&18	ADC25&26
				
			Sample 150		Channel 2&4	ADC7&8	ADC15&16	ADC23&24		ADC31&32	
	SRC2, WL1&2							SRC1, WL3&4			
		SRC2, WL1&2	Sample 1	Channel 1&3	ADC1&2	ADC9&10	ADC17&18	ADC25&26			
					
			Sample 150	Channel 2&4	ADC7&8	ADC15&16	ADC23&24	ADC31&32			
			
	SRC32, WL3&4										
		SRC32, WL3&4	Sample 1	Channel 1&3	ADC1&2	ADC9&10	ADC17&18	ADC25&26			
					
			Sample 150	Channel 2&4	ADC7&8	ADC15&16	ADC23&24	ADC31&32			
								SRC32, WL3&4			

Fig. 4 Detailed timing sequence outlining the synchronization between the optical switch, ADC, and DSP to acquire one frame of data.

Once the DSPs have received 150 samples from all 128 detectors, the mDSP signals to the mCPLD to change the source position and begins the 7 ms pause waiting for the switch to settle. During that settling time, the speed of the system is optimized by having the DSPs run the lock-in detection on the samples from the previous source before sending them out to the host computer. In addition, while the optical switch is settling on the new source position, the gain bits are updated, and the analog electronics have time to settle.

2.3 Host Computer and User Interface

The host computer uses a LabVIEW graphical user interface (GUI) to facilitate communication with the hardware. The system can be configured through the GUI to run with an arbitrary number of sources and detectors and wavelengths. The GUI gives the user the ability to manually configure the gain settings for each source-detector pair, but also provides the ability to automatically test and select optimal gain settings for each source and detector. Once the optimal gain settings are selected, the imaging screen provides the ability to start, pause, and stop imaging. It also shows the real-time traces of the detector signals for a given source and wavelength. Screen shots of the user interface to control the gain bit settings and the image acquisition are shown in Fig. 5.

3 Instrument Performance

3.1 System Timing

This system was designed for dynamic breast imaging, making the dynamic range and the speed of acquisition two of the primary criteria. The temporal response, as described in detail in Sec. 2.2.4, is limited by the settling time of the optical switch and the number of source positions and wavelengths. The switch requires 7 ms to settle after switching positions, followed by 2 ms to acquire the data for all detectors at that source position. This brings the imaging time to 9 ms per source position. Since we sequentially image the two wavelength sets, the imaging rate also depends on the number of wavelengths. Consequently, the fastest that the system can image is to collect one frame in 0.009 s with one source and two wavelengths (111 Hz). Or, with 32 sources and two wavelengths it can acquire a frame in 0.288 s (3.5 Hz). Finally, the slowest configuration is to use all 32 sources and four wavelengths, in which case it takes 0.576 s to acquire one frame (1.7 Hz).

3.2 Dark Noise

The dark noise is the measured signal when no incident light is present, and thus represents the smallest measurement that can be reliably made with the system. Figure 6 shows the dark

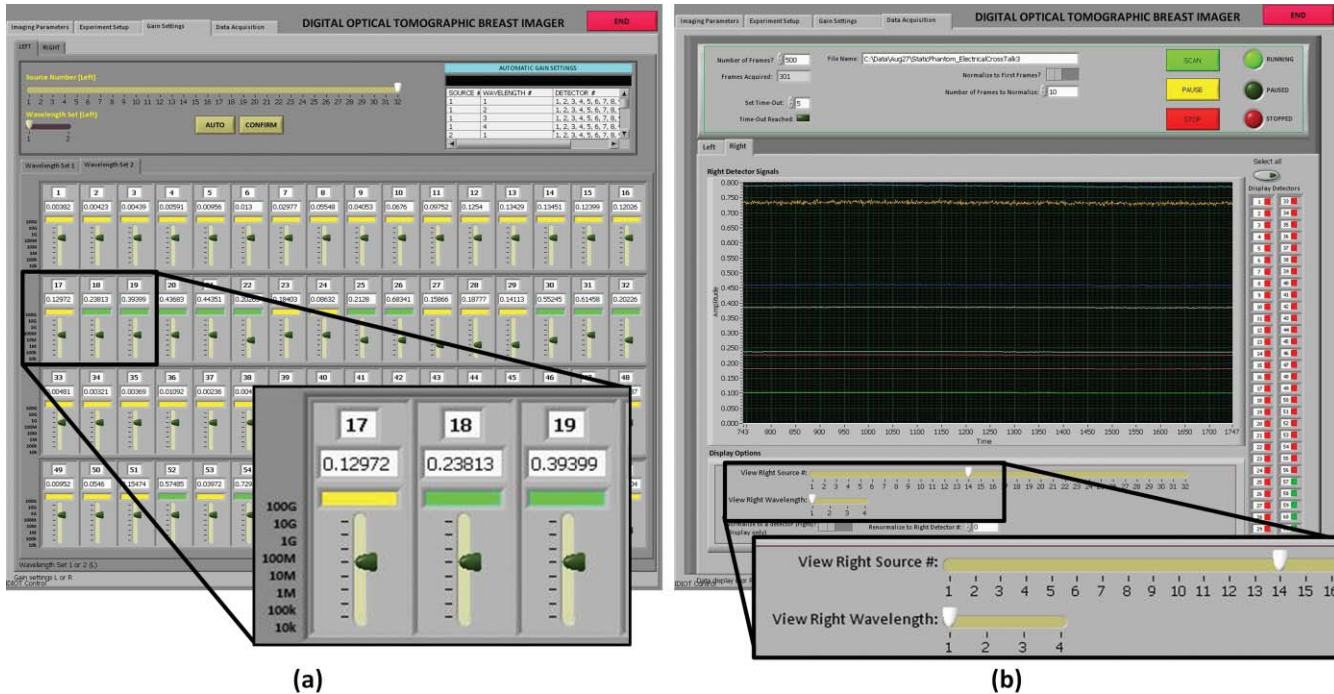


Fig. 5 Screenshots of the LabVIEW user interface to (a) control the gain bits for each source-detector pair and (b) visualize the raw data as it is acquired.

noise measured for each gain setting with the standard deviation of the measurements across all detectors indicated by the error bars. As expected, with increasing amplification in the PGA stage, and eventually in the TIA stage, we see increasing noise present. At the lower gain stages we see noise levels below 50 μV , but as the gain increases we see increasing noise; until at the highest gain stage of 10 GV/A, we have an RMS dark noise of 22 mV. The slightly higher noise at the 1 M versus the 10 M setting represents the fact that the 1 M setting uses less TIA gain and more PGA gain, whereas the 10 M setting uses more TIA gain and less PGA gain. While TIA gain improves the SNR, PGA gain does not. This finding demonstrates that increasing the gain at the TIA stages is preferred over increasing the gain at the PGA stage.

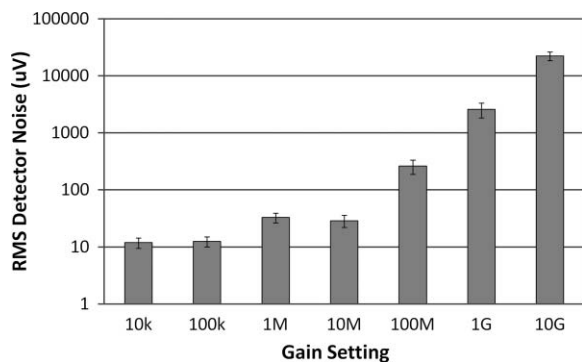


Fig. 6 Logarithmic plot of the RMS dark noise for each detector gain setting.

3.3 Noise Equivalent Power and Dynamic Range

The noise equivalent power (NEP) is an indication of the detector sensitivity to light and can be computed for an SNR of unity using the dark noise of the highest gain setting. Taking the mean of the root-mean-squared (RMS) detector noise at the highest gain setting and using the known properties of the silicon photodetector in the given wavelength range of 0.5 W/A, we calculate that the NEP is approximately 4.5 pW RMS. The NEP represents the smallest light signal that can be detected. The largest light signal that can be detected uses the full detector range for the lowest gain setting, which in this case is to detect 2.5 V peak-to-peak on the 10 kV/A gain setting. Using these values we can calculate the dynamic range of the system to be 10^8 (or 158 dB).

3.4 Coefficient of Variation and Long Term Stability

The coefficient of variation (CV) is calculated here for a static breast-shaped phantom with breast optical properties over a period of five minutes (500 frames) with the full number of sources and detectors. Figure 7 shows the mean of the CV calculated for all detectors at the given gain setting for each wavelength. Up until 100 MV/A, the CV is as low as 0.15% for some wavelengths but by the highest gain setting it increases to approximately 3%. The SNR for each of these settings can be calculated as $20\log_{10}(1/\text{CV})$ giving us an average SNR of 51 dB for the lowest gain setting and 30 dB for the highest gain setting.

To assess the long term stability of the system, we measured the same static breast phantom over 40000 frames (~ 38 min). Taking the mean of measured values at frame 1 and calculating the percentage change between that and the mean at frame 40000, there is a 0.7% change in the measured value.

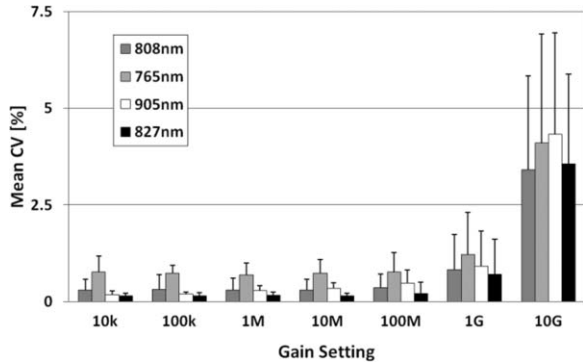


Fig. 7 Mean CV of the detectors at each gain setting for each wavelength with standard deviation error bars.

3.5 System Linearity

System linearity was examined by using the same incident light on a detector and then measuring the detected voltage across all possible gain settings. This was repeated four times in order to cover all gain settings and the results are plotted in Fig. 8, where we see that a linear relationship across the gain settings is generally maintained. We expect to see a 10× gain factor between each gain setting measuring the same signal. An exponential fit of the data in Fig. 8 should give an equation of $e^{-2.3}$ in a perfectly linear 10× relationship between gain settings. For the curves below, we see good linearity with fits of $e^{-2.31}$ ($R = 1$), $e^{-2.27}$ ($R = 0.9999$), $e^{-2.30}$ ($R = 1$), and $e^{-2.02}$ ($R = 0.9955$) for S1 through S4. We expect the decreased linearity at the highest gain settings (reflected by S4), since those settings also introduce higher noise levels.

3.6 System Summary and Discussion

The various system characteristics are summarized in Table 3. Shown in Fig. 9, the system is on a portable cart with wheels (104 cm × 79 cm × 66 cm) and draws 3.5 Amps of current at 120 V AC. These features make it a portable low-power device suitable for use in a clinical setting.

Table 4 presents a comparison between the new digital breast and the original digital imaging systems previously presented.³⁴ The most important difference between these systems lies in the dramatic increase in sources, detectors, and wavelengths for the

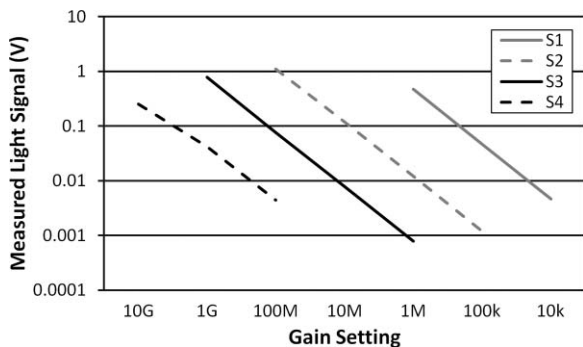


Fig. 8 Linearity across all gain settings measured through four samples (S1 to S4) covering all settings. Each sample reflects the same input intensity measured across multiple gain settings.

Table 3 Summary of system characteristics.

Parameter	Value
Sources	32 per breast, 64 total
Detectors	64 per breast, 128 total
Wavelengths	<5 mW at 765 nm, <5 mW at 808 nm, <5 mW at 827 nm, <5 mW at 905 nm
Temporal response	111 Hz (1 source, 2 wavelengths), 3.5 Hz (32 sources, 2 wavelengths), 1.7 Hz (32 sources, 4 wavelengths)
Dynamic range	~ 10 ⁸ (158 dB)
Noise equivalent power	~ 4.5 pW RMS
Dark noise amplitude	<10 μV RMS (at lowest gain setting), <22 mV RMS (at highest gain setting)
Long term stability	0.7% over 40 min
System size	104 cm × 79 cm × 66 cm
Power consumption	3.5 Amps @ 120 V AC



Fig. 9 Photograph of the digital DOT system.

Table 4 Comparison of system characteristics for the first generation digital imager and the second generation digital breast imager.

Parameter	Digital imager (Ref. 34)	Digital breast imager
Mode of operation	CW	CW
Sources	16	64
Detectors	32	128
Wavelengths	1 to 2	1 to 4
Total data points	1024	16,384
Frame rate	8.9 to 140 Hz	1.7 to 111 Hz
Dynamic range	~180 dB	~160 dB
Dark noise	20 to 400 μ V	10 μ V to 22 mV
CV (%)	0.05 to 0.5%	0.3 to 3%
Number of DSP chips	1	4
System size (including cart)	81 \times 61 \times 64 cm	104 \times 79 \times 66 cm

application to breast imaging, bringing the number of data points collected per frame from 1024 in the original system to 16384 in the breast imaging system. Despite this 16-fold increase in data, there is only a five-fold decrease in system speed, from 8.9 to 1.7 Hz. In fact, the decrease in imaging speeds primarily comes from the increased number of sources and wavelengths, and not from the four-fold increase in detectors. This is accomplished by the new master-slave architecture implemented for simultaneous data detection and demodulation from 128 detectors. In addition, despite the large increase in detectors, sources, and wavelengths, the size of the entire breast imaging system (including the cart) is only slightly larger than the original digital imaging system. This is due to more compact digital detection boards (eight channels per board as opposed to four) as well as the master-slave DSP-based architecture that can scale effortlessly with the number of detectors.

The breast imaging system uses less low-gain settings and adds more high-gain settings to handle the larger imaging volumes. This accounts for the lower dynamic range as well as the fact that the higher-gain settings lead to slightly higher dark noise and CV%, as expected. Overall, the system performance is similar between the two systems as they are based upon the same detection techniques – both have coefficients of variation of less than 1% for most gain settings and have very low dark noise (<50 μ V for most gain settings).

4 Image Reconstruction

Three dimensional reconstructions are performed for the measurement data by using a recently developed partial-differential-equation (PDE) constrained multispectral imaging method.⁴⁰ In the following, we provide a brief description of this method, in-

cluding the diffusion approximation as a light propagation model and the PDE-constrained inverse model of directly recovering chromophore concentrations in tissue.

Light propagation in scattering-dominant media such as breast tissue is well described by the diffusion approximation (DA) to the equation of radiative transfer as:

$$-\nabla \cdot D(\vec{\mathbf{r}})\nabla u(\vec{\mathbf{r}}) + \mu_a u(\vec{\mathbf{r}}) = f(\vec{\mathbf{r}}) \text{ in } X \text{ s.t. } u(\vec{\mathbf{r}}) + 2D(\vec{\mathbf{r}})A \frac{\partial u(\vec{\mathbf{r}})}{\partial \vec{n}} = 0 \text{ in } \partial X, \quad (2)$$

where A is related to reflection due to mismatched refractive indices, $u(\vec{\mathbf{r}})$ is the radiation density, and $D(\vec{\mathbf{r}})$ is the diffusion coefficient given by $D = 1/(3(\mu_a + \mu'_s))$. The solution to Eq. (2) provides a prediction $P_\lambda = Qu_\lambda$ of the measurement at the medium surface, where Q represents a measurement operator that projects the forward solution $u(\vec{\mathbf{r}})$ onto the measurable quantity by our digital dynamic imaging system. The basic idea behind DOT imaging of tissue chromophores is to exploit the linear correlation between the tissue absorption and the concentrations of chromophores in tissue as

$$\mu_a(\lambda) = \sum_{i=1}^{N_c} \varepsilon_i(\lambda)C_i, \quad (3)$$

where $\varepsilon_i(\lambda)$ and C_i are the absorption extinction coefficient and the concentration, respectively, for the i th chromophore in tissue, and N_c is the number of total chromophores that contribute to the absorption at wavelength λ . The major chromophores relevant to breast imaging are oxygenated hemoglobin (HbO_2), deoxygenated hemoglobin (Hb), water (H_2O) and lipid, whose molar extinction coefficients are well documented in the literature.⁴¹ The multispectral inverse model can directly recover the spatial distributions of chromophore concentrations by simultaneously using data from all wavelengths during the reconstruction.⁴² This is achieved here with the following Lagrangian formulation for PDE-constrained multispectral optimization:

$$L(x, u_\lambda; \eta_\lambda) = \frac{1}{2} \sum_{\lambda} |Qu_\lambda - z_\lambda^{\text{obs}}|^2 + \beta R + \sum_{\lambda} \eta_\lambda^T (Au_\lambda - b). \quad (4)$$

Here, x is a vector of all unknown chromophores that may include [HbO_2], [Hb], [H_2O], or [Lipid] concentrations, $Au = b$ is a system of discretized diffusion equations, z_λ is the measurement at wavelength λ , and β is a regularization parameter that controls a strength of smoothing R . Instead of a classical Tikhonov-type regularization, we employed here a radial basis function-type smoothing operator since it performs better on a grid of unstructured meshes.⁴³ We solve this PDE-constrained multispectral inverse problem within a framework of the reduced Hessian sequential quadratic programming method (rSQP) that accelerates the reconstruction process.⁴⁴

The rSQP method finds the next step $p = (\Delta x, \Delta u)$ through the minimization to a quadratic approximation of the Lagrangian function L subject to the linearized constraints:

$$\begin{aligned} \min \quad & \Delta x^{kT} g_r^k + \frac{1}{2} \Delta x^{kT} H_r^k \Delta x^k \\ \text{subject to} \quad & C^k \Delta p^k + (Au_\lambda - b)^k = 0, \end{aligned} \quad (5)$$

where g^k is the reduced gradient and H^k is the reduced Hessian of the Lagrangian function. Here C^k denotes the Jacobian matrix of the DA with respect to $p = (x, u)$, given by $C^k = (Au_\lambda - b)_p^{kT}$. With the solutions of the quadratic problem (5), we finally obtain the new iterates for both the forward and inverse variables in each step of optimization as

$$\begin{aligned} x^{k+1} &= x^k + \alpha^k \Delta x^k \\ u_\lambda^{k+1} &= u_\lambda^k + \alpha^k \Delta u_\lambda^k, \end{aligned} \quad (6)$$

where α^k is the step length chosen through a line search. The reduced-space formulation is described in detail by Kim et al.⁴⁴

The method described in Eqs. (2)–(6) is used for our clinical study involving the reconstruction of chromophores concentrations in breast tissue. In this experimental study, we focus on the reconstruction of two major chromophores concentrations, i.e., [HbO₂] and [Hb], by using data from two wavelengths ($\lambda = 765$ and 835 nm) since these two chromophores are closely associated with a variety of physiological processes. Also, it should be noted that the reconstructed hemoglobin concentrations are the differences relative to the concentrations at the reference state; therefore, all images that will be shown next indicate the concentration difference in percentage change from baseline [%]. To this end, we made an assumption of the homogeneous concentrations of [HbO₂] and [Hb] for the baseline state in which the [HbO₂] and [Hb] concentrations are set to 18 and 9 [μ M],

respectively. These values represent typical values for breast tissue. While the baseline [HbO₂] and [Hb] may vary by patient, it has been shown that the reconstruction of dynamic measures is far less sensitive to inaccuracies in the reference values when compared to the reconstruction of absolute measures.⁴⁵ Note that effects of other chromophores such as H₂O and lipid are not considered in this study. Under this assumption, we generated the forward prediction P_{ref}^λ for the reference state first and then used this prediction data to obtain the difference data as

$$z_{tar}^\lambda = \frac{M_{tar}^\lambda}{M_{ref}^\lambda} P_{ref}^\lambda, \quad (7)$$

where M_{tar}^λ and M_{ref}^λ denote the spectral measurements at wavelength λ for the target state of unknown optical properties and for the reference state of assumed optical properties, respectively. This calibrated difference data is used as input to the reconstruction code; however, any data with an SNR below 15 dB was excluded from the reconstruction since this data may cause potential numerical instability or produce artifacts in the reconstruction image. The baseline data from 30 s (50 frames) prior to the onset of the breath hold was averaged and used as the reference state.

A typical three dimensional (3D) volume mesh as shown in Fig. 10(a) is covered by approximately 6500 tetrahedron elements. The total reconstruction time for a single frame is under

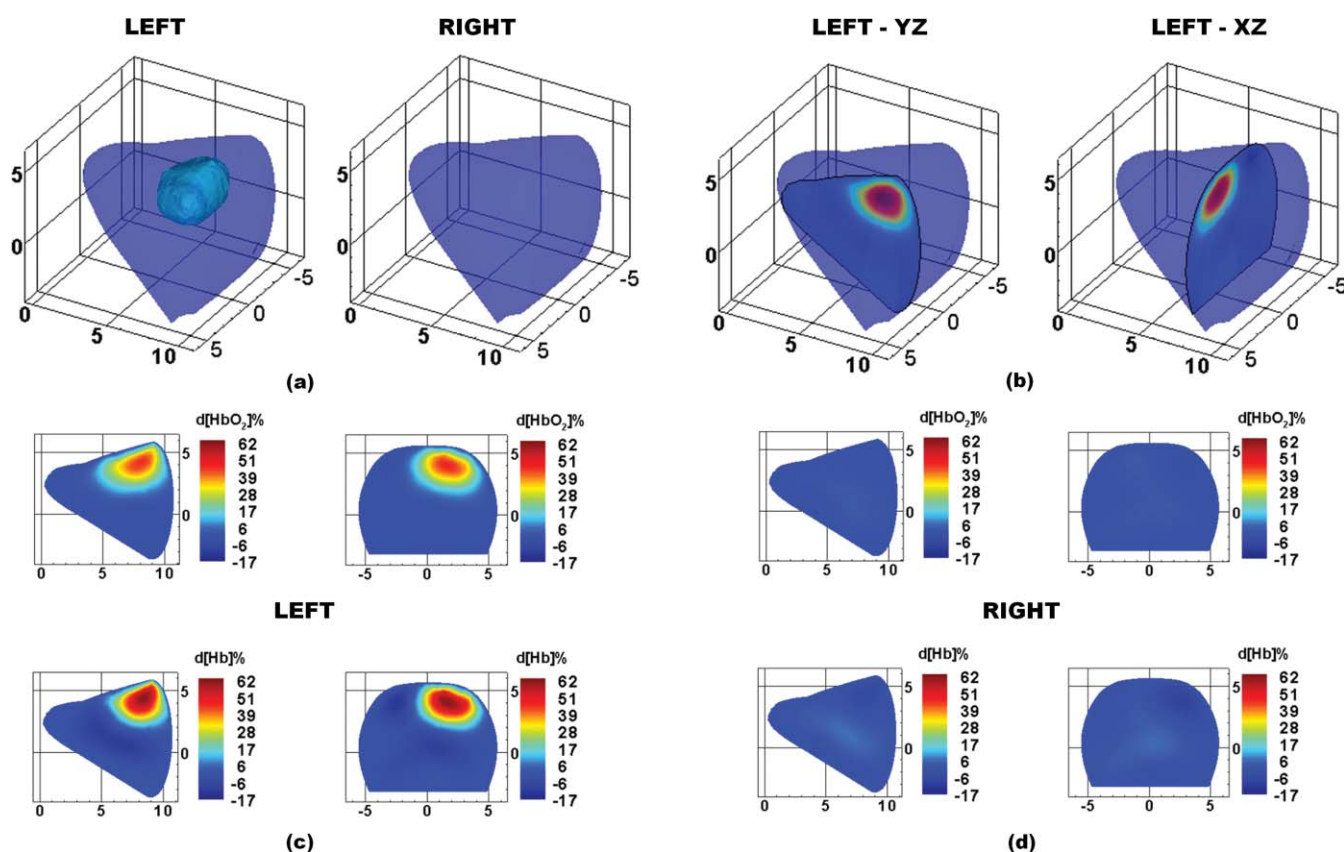


Fig. 10 DOT images for case study 1, a $1.8 \times 1.5 \times 1.9$ cm carcinoma in the left breast. (a) 3D isosurface taken at 18% d[Hb] identifies the tumor region in the left breast. (b) Location of 2D slices extracted from the 3D reconstruction. Finally, the 2D maps of d[HbO₂] (top row) and d[Hb] (bottom row) are shown for the (c) left and (d) right breasts.

10 min on a Dual Core Intel Xeon 3.33 GHz processor. DOT images were compared with mammograms and ultrasound images of the same breast to determine the actual location and size of the tumor.

5 Clinical Results

5.1 Experimental Protocol

To illustrate the performance of the system in a clinical setting, we gathered preliminary imaging data from two breast cancer patients and one healthy volunteer. Prior to the measurements, each participant was trained on how to perform a valsalva breath hold by maintaining pressure in their mouth and lower abdomen. Participants were also informed about the importance of minimizing motion during the imaging sequences. The valsalva maneuver is a commonly used tool in a number of clinical diagnoses including many cardiac and brain abnormalities.^{46,47} It involves a prolonged expiratory effort that results in increased intra-thoracic pressure, which results in decreased venous return to the heart. It is expected that this decrease in venous return will correlate to a measurable increase in hemoglobin levels in the breast tissue as shown by Schmitz et al.²⁶ Hemoglobin levels are relevant to the detection of breast cancer because they provide contrast between normal tissue vascularization and increased disorderly tumor vascularization.

During the measurements, the patient was asked to stand in a comfortable position while the imaging interface was brought into contact with the breast. Each fiber-bearing finger of the interface was adjusted until gentle contact with the breast was established for all fibers, starting with the outer fingers and progressing to the center fingers. During this time, the patient was asked to identify any fibers that were causing discomfort, and such fibers were then readjusted.

In order to minimize the patient's discomfort and the risk of motion artifacts, the imaging sequence was kept as short as possible, while still maintaining time for the dynamic effects to settle. The imaging sequence involved a 90-second baseline followed by a 30-second breath hold and 90-second recovery, which was repeated three times. This resulted in a total imaging duration of approximately 10 min. All images shown in this paper are extracted from the second of the three trials. By the second trial the patient had settled into the protocol and there was generally less motion as compared to the third trial. The experimental protocol was approved by the Institutional Review Board at Columbia University and informed consent was obtained from all subjects prior to imaging.

5.2 Imaging Results

In all cases presented here, we have selected a frame 15 s following the 30-second breath-hold as we found that this protocol

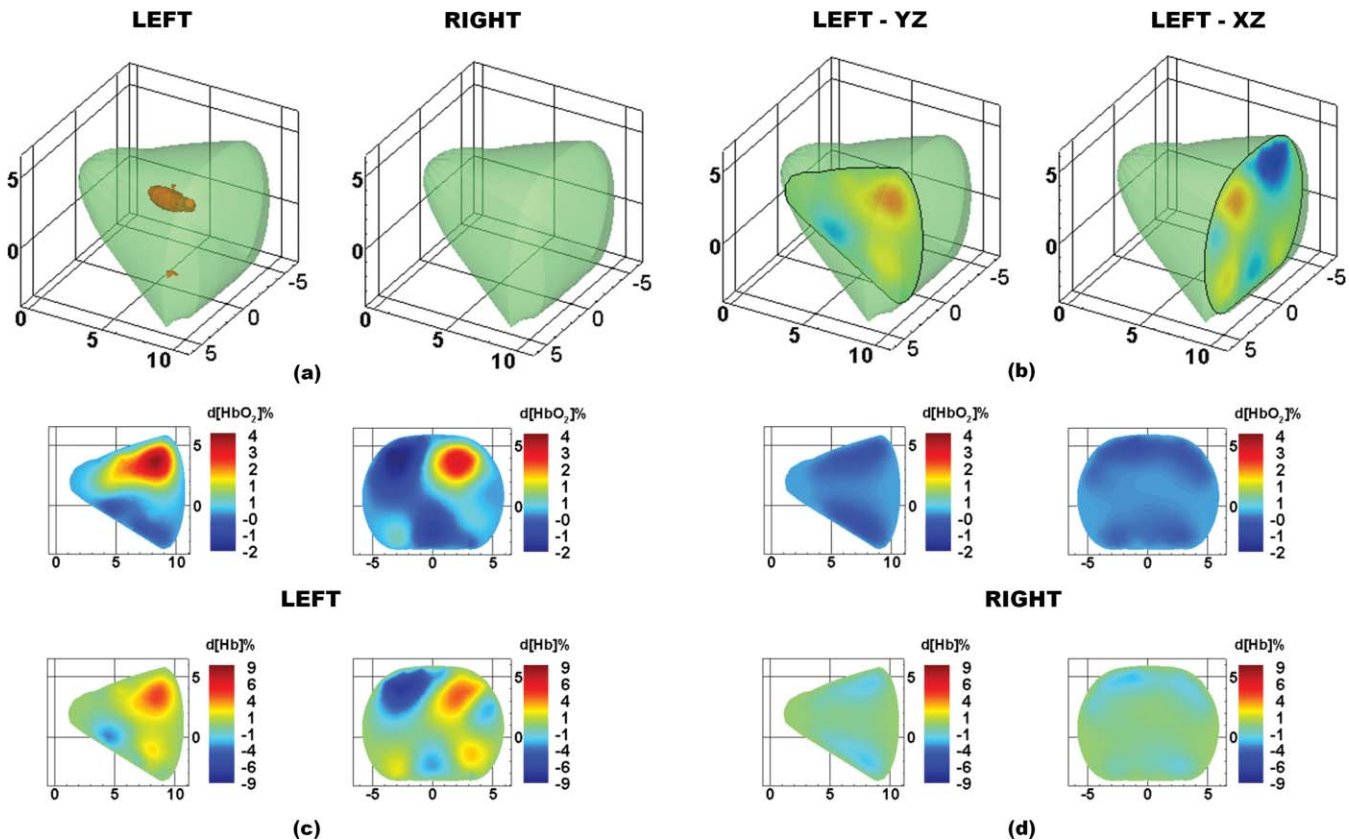


Fig. 11 DOT images for case study 2, a 2.1 × 1.8 × 2.0 cm carcinoma in the left breast. (a) 3D isosurface taken at 4% d[Hb] identifies the tumor region in the left breast. (b) Location of 2D slices extracted from the 3D reconstruction. Finally, the 2D maps of d[HbO₂]% (top row) and d[Hb]% (bottom row) are shown for the (c) left and (d) right breasts.

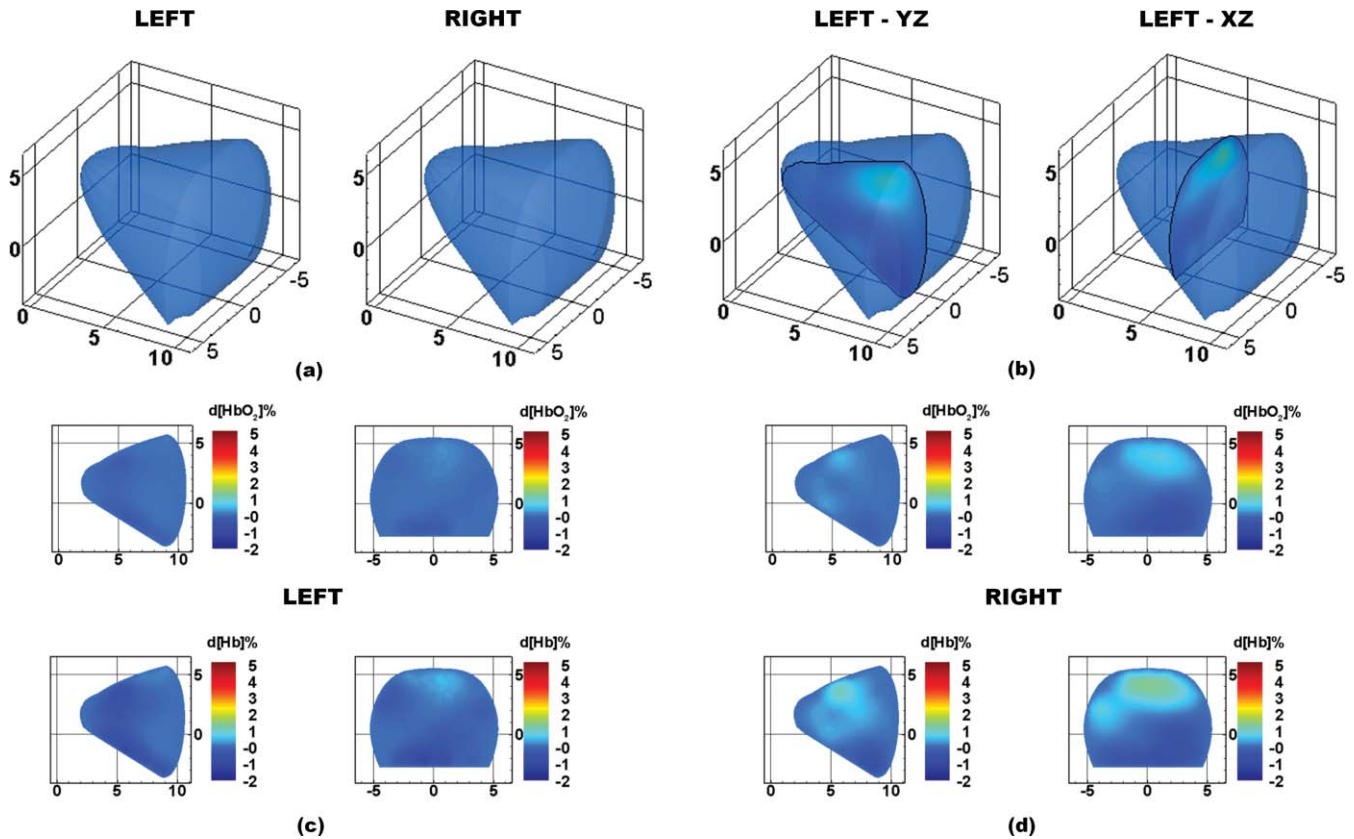


Fig. 12 DOT images for case study 3, a healthy patient. (a) 3D isosurface taken at 3% d[Hb] identifies no tumor region in either breast. (b) Location of 2D slices extracted from the 3D reconstruction. Finally, the 2D maps of d[HbO₂]% (top row) and d[Hb]% (bottom row) are shown for the (c) left and (d) right breasts.

allowed us to best visualize the differences in the dynamic response between the tumor and healthy tissues.

5.2.1 Case study 1: 2-cm carcinoma

The first case is a 49 year-old premenopausal female with a body mass index (BMI) of 29.2. The patient presented with a $1.8 \times 1.5 \times 1.9$ cm mass in the posterior third mid outer quadrant of the left breast at the 3:00 axis as identified by mammography and sonography. Biopsy pathology showed a moderately differentiated ductal carcinoma and tubulolobular carcinoma.

Figure 10 shows optical tomographic images of the breasts at 15 s after the completion of the breath hold. A 3D isosurface drawn at 18% d[Hb] identifies the tumor in the correct region of the left breast [Fig. 11(a)]. From a cross-section through the breasts in the sagittal yz -plane (at $x = 2$ cm) and coronal xz -plane (at $y = 7.5$ cm) the tumor location can be visualized in two dimensions [Fig. 10(b)]. Maps of the change in oxygenated hemoglobin (d[HbO₂]%) and deoxygenated hemoglobin (d[Hb]%) clearly identify a region of increased hemoglobin levels in the tumor-bearing left breast [Fig. 10(c)], but no such regions in the healthy right breast [Fig. 10(d)]. These images demonstrate that the vasculature in the tumor region is more sluggish in its recovery from the breath hold, providing a window of contrast 15 s into the recovery period. The right

breast shows a relatively homogeneous return to baseline at 15 s into the recovery period, as does the healthy tissue surrounding the tumor in left breast.

5.2.2 Case study 2: 2-cm carcinoma

The second patient is a 58 year-old premenopausal female with a BMI of 28.7. The patient presented with a $2.1 \times 1.8 \times 2.0$ cm mass located in the left breast at 2:30, 10 cm from the nipple, as identified by targeted sonography. Biopsy pathology showed an invasive ductal carcinoma with lobular features.

Figure 11 shows optical tomographic images of the breasts at 15 s after the completion of the breath hold. A 3D isosurface drawn at 4% d[Hb] identifies the tumor in the correct region of the left breast [Fig. 11(a)]. From a cross-section through the breasts in the sagittal yz -plane (at $x = 2$ cm) and coronal xz -plane (at $y = 9$ cm), the tumor location can be visualized in two dimensions [Fig. 11(b)]. Maps of d[HbO₂]% and d[Hb]% clearly identify a region of increased hemoglobin levels in the tumor-bearing left breast [Fig. 11(c)], but no such regions in the healthy right breast [Fig. 11(d)]. Similar to case study 1 (Fig. 10), these reconstructed images demonstrate that the tumor region is more sluggish in its recovery from the breath hold and can be identified by its increased d[HbO₂]% and d[Hb]% at the frame 15 s following the end of the breath hold.

5.2.3 Case study 3: healthy patient

The third patient is a healthy 41 year-old premenopausal female with a BMI of 22.6. Figure 12 shows optical tomographic images of the breasts at 15 s after the completion of the breath hold. A 3D isosurface drawn at 3% d[Hb] identifies no suspicious regions in either breast [Fig. 12(a)]. From a cross-section through the breasts in the sagittal yz -plane (at $x = 1.5$ cm) and coronal xz -plane (at $y = 6$ cm), the breast chromophores can be visualized in 2D [Fig. 12(b)]. Maps of the change in d[HbO₂] % and d[Hb] % are very homogeneous in both breasts with no regions of significantly increased hemoglobin [Figs. 12(c) and 12(d)]. These results demonstrate that by imaging during the recovery period from a breath hold, tumor regions in breast cancer patients are identified, but not in healthy subjects.

5.3 Discussion

In three subjects we explored the use of a breath hold as a method for creating dynamic contrast for distinguishing healthy from cancerous tissue. The onset of a valsalva breath hold causes an increase in venous return pressure that consequently results in an increase in hemoglobin in the breast.^{26,48} Once the subject begins breathing again the hemoglobin levels return to baseline. However, the return of the hemoglobin levels to baseline is much more sluggish in the tumor region than in the healthy tissue. As a result, by capturing images during the recovery period following the breath hold, we can visualize the tumor region by its increased hemoglobin levels.

The unique transient response observed in the tumor region is caused by its unusual vascular structure. Due to excess endothelial cells and abnormal perivascular cells, tumor vasculature is disorganized and hyperpermeable.²⁵ Abnormal vascular architecture, common in solid tumors, is known to increase the resistance to blood flow through the tumor.⁴⁹ The inefficient transport of blood to and from the tumor affects the hemodynamic response of the tumor area and results in the sluggish transient recovery observed here. In the healthy subject, both breasts showed uniform recovery following the breath hold, whereas in the two subjects with breast tumors, the tumor-bearing breast had regions of delayed hemoglobin recovery that correlated with the tumor location. These physiological findings correlate with a study by Schmitz et al. who also looked at the transient response of tumors to a valsalva maneuver.²⁶

While these preliminary studies suggest that the transient response of tissue may be a valuable tool for breast cancer detection, it is clear that more studies are required to fully understand the clinical significance of this technique. An important part of these future studies will be the identification of the most reliable and reproducible way to identify tumor regions. In the presented preliminary cases, we found a range in the optimal isosurface values for visualizing the tumor region (18 and 4% increases in d[Hb] % in case studies 1 and 2, respectively). The selection of threshold values could potentially be generalized by first normalizing to the peak percentage change in d[HbO₂] % and d[Hb] % images and subsequently looking for the same fractional increase in all cases. Data from the healthy contra-lateral breast can also be used to normalize the data. By designing a prototype imager and showing some case studies, we have

taken the first step toward the exploration of dynamic imaging methods in larger clinical trials.

6 Summary

We have presented a new CW DOT breast imaging system suitable for clinical implementation that uses a DSP based architecture to collect a large amount of imaging data at high frame rates. This system builds upon the design of an earlier instrument that used 16 sources, 32 detectors with two wavelengths, and that could image at speeds of up to 9 Hz.³⁴ The new breast imaging system extends that design to a multiple DSP detection architecture that coordinates the data acquisition and processing by using a master-slave architecture. This approach increases the number of sources and detectors to 32 sources and 64 detectors per breast (64 sources, 128 detectors total) with four wavelengths while still maintaining frame rates of 1.7 Hz. The increased number of sources and detectors can accommodate the larger geometries required for simultaneous breast imaging, with fast imaging rates (1.7 to 111 Hz depending on the number of sources and wavelengths) and a large dynamic range (10^8). Furthermore, the new master-slave DSP architecture is scalable, allowing for increased numbers of sources, wavelengths, or detectors without significantly increasing the system size or cost.

We employed the new system to image the breasts of two cancer patients and one healthy volunteer. We showed that a simple breath hold can be used to detect tumors by their hemodynamic responses. In particular, we found that oxy- and deoxyhemoglobin levels in tumors take longer to return to baseline after a breath hold than in normal tissue. In future studies we will explore the use of the new system to imaging dynamic responses to other perturbations such as indocyanine green injections, pressure application to the breast, or gas inhalation.

Acknowledgments

This research was supported by the National Institutes of Health (R41CA096102), the US Army (DAMD017-03-C-0018), the Susan G. Komen Foundation, the New York State Office of Science, and Technology and Academic Research (NYSTAR – Technology Incentive Program C020041) and NIRx Medical Technologies. Furthermore, Molly Flexman is supported in part by the Natural Sciences and Engineering Research Council of Canada (NSERC). The authors would like to thank Andres Bur, Yang Li, James Masciotti, and Alisha Ling for their help with the instrumentation. The authors would also like to thank the volunteers and the recruitment coordinator Maria Alvarez-Cid, without whom the clinical portion of this research would not have been possible.

References

1. S. F. Altekruze, C. L. Kosary, M. Krapcho, N. Neyman, R. Aminou, W. Waldron, J. Ruhl, N. Howlader, Z. Tatalovich, H. Cho, A. Mariotto, M. P. Eisner, D. R. Lewis, K. Cronin, H. S. Chen, E. J. Feuer, D. G. Stinchcomb, and B. K. Edwards, "SEER Cancer Statistics Review 1975–2007," http://seer.cancer.gov/csr/1975_2007/ (2010).
2. A. Jemal, R. Siegel, J. Q. Xu, and E. Ward, "Cancer Statistics, 2010," *Ca-Cancer J. Clin.* **60**(5), 277–300 (2010).
3. J. G. Elmore, K. Armstrong, C. D. Lehman, and S. W. Fletcher, "Screening for breast cancer," *J. Am. Med. Assoc.* **293**(10), 1245–1256 (2005).

4. J. G. Elmore, M. B. Barton, V. M. Mocerri, S. Polk, P. J. Arena, and S. W. Fletcher, "Ten-year risk of false positive screening mammograms and clinical breast examinations," *N. Engl. J. Med.* **338**(16), 1089–1096 (1998).
5. B. J. Tromberg, B. W. Pogue, K. D. Paulsen, A. G. Yodh, D. A. Boas, and A. E. Cerussi, "Assessing the future of diffuse optical imaging technologies for breast cancer management," *Med. Phys.* **35**(6), 2443–2451 (2008).
6. D. R. Leff, O. J. Warren, L. C. Enfield, A. Gibson, T. Athanasiou, D. K. Patten, J. Hebden, G. Z. Yang, and A. Darzi, "Diffuse optical imaging of the healthy and diseased breast: a systematic review," *Breast Cancer Res. Treat.* **108**(1), 9–22 (2008).
7. R. A. Weinberg, *The Biology of Cancer*, Garland Science, Taylor & Francis Group, London (2007).
8. I. J. Bigio, S. G. Bown, G. Briggs, C. Kelley, S. Lakhani, D. Pickard, P. M. Ripley, I. G. Rose, and C. Saunders, "Diagnosis of breast cancer using elastic-scattering spectroscopy: preliminary clinical results," *J. Biomed. Opt.* **5**(2), 221–228 (2000).
9. J. R. Mourant, J. P. Freyer, A. H. Hielscher, A. A. Eick, D. Shen, and T. M. Johnson, "Mechanisms of light scattering from biological cells relevant to noninvasive optical-tissue diagnostics," *Appl. Opt.* **37**(16), 3586–3593 (1998).
10. J. Wang, S. D. Jiang, Z. Z. Li, R. M. diFlorio-Alexander, R. J. Barth, P. A. Kaufman, B. W. Pogue, and K. D. Paulsen, "In vivo quantitative imaging of normal and cancerous breast tissue using broadband diffuse optical tomography," *Med. Phys.* **37**(7), 3715–3724 (2010).
11. L. C. Enfield, A. P. Gibson, N. L. Everdell, D. T. Delpy, M. Schweiger, S. R. Arridge, C. Richardson, M. Keshtgar, M. Douek, and J. C. Hebden, "Three-dimensional time-resolved optical mammography of the uncompressed breast," *Appl. Opt.* **46**(17), 3628–3638 (2007).
12. P. Taroni, A. Torricelli, L. Spinelli, A. Pifferi, F. Arpaia, G. Danesini, and R. Cubeddu, "Time-resolved optical mammography between 637 and 985 nm: clinical study on the detection and identification of breast lesions," *Phys. Med. Biol.* **50**(11), 2469–2488 (2005).
13. H. Rinneberg, D. Grosenick, K. T. Moesta, H. Wabnitz, J. Mucke, G. Wubbeler, R. Macdonald, and P. Schlag, "Detection and characterization of breast tumours by time-domain scanning optical mammography," *Opto-Electron. Rev.* **16**(2), 147–162 (2008).
14. X. Intes, "Time-domain optical mammography softscan: initial results," *Acad. Radiol.* **12**(8), 934–947 (2005).
15. R. Choe, S. D. Konecky, A. Corlu, K. Lee, T. Durduran, D. R. Busch, S. Pathak, B. J. Czerniecki, J. Tchou, D. L. Fraker, A. DeMichele, B. Chance, S. R. Arridge, M. Schweiger, J. P. Culver, M. D. Schnall, M. E. Putt, M. A. Rosen, and A. G. Yodh, "Differentiation of benign and malignant breast tumors by in-vivo three-dimensional parallel-plate diffuse optical tomography," *J. Biomed. Opt.* **14**(2), 024020 (2009).
16. S. Srinivasan, B. W. Pogue, S. Jiang, H. Dehghani, C. Kogel, S. Soho, J. J. Gibson, T. D. Tosteson, S. P. Poplack, and K. D. Paulsen, "In vivo hemoglobin and water concentrations, oxygen saturation, and scattering estimates from near-infrared breast tomography using spectral reconstruction," *Acad. Radiol.* **13**(2), 195–202 (2006).
17. X. P. Liang, Q. Z. Zhang, C. Q. Li, S. R. Grobmyer, L. L. Fajardo, and H. B. Jiang, "Phase-contrast diffuse optical tomography: pilot results in the breast," *Acad. Radiol.* **15**(7), 859–866 (2008).
18. S. van de Ven, S. G. Elias, A. J. Wiethoff, M. van der Voort, T. Nielsen, B. Brendel, C. Bontus, F. Uhlemann, R. Nachabe, R. Harbers, M. van Beek, L. Bakker, M. B. van der Mark, P. Luijten, and W. Mali, "Diffuse optical tomography of the breast: preliminary findings of a new prototype and comparison with magnetic resonance imaging," *Eur. Radiol.* **19**(5), 1108–1113 (2009).
19. J. Wang, B. W. Pogue, S. D. Jiang, and K. D. Paulsen, "Near-infrared tomography of breast cancer hemoglobin, water, lipid, and scattering using combined frequency domain and cw measurement," *Opt. Lett.* **35**(1), 82–84 (2010).
20. Q. Q. Fang, S. A. Carp, J. Selb, G. Boverman, Q. Zhang, D. B. Kopans, R. H. Moore, E. L. Miller, D. H. Brooks, and D. A. Boas, "Combined optical imaging and mammography of the healthy breast: optical contrast derived from breast structure and compression," *IEEE Trans. Med. Imaging* **28**(1), 30–42 (2009).
21. N. G. Chen, P. Y. Guo, S. K. Yan, D. Q. Piao, and Q. Zhu, "Simultaneous near-infrared diffusive light and ultrasound imaging," *Appl. Opt.* **40**(34), 6367–6380 (2001).
22. S. S. You, Y. X. Jiang, Q. L. Zhu, J. B. Liu, J. Zhang, Q. Dai, H. Liu, and Q. Sun, "US-guided diffused optical tomography: a promising functional imaging technique in breast lesions," *Eur. Radiol.* **20**(2), 309–317 (2010).
23. B. Brooksby, S. D. Jiang, H. Dehghani, B. W. Pogue, K. D. Paulsen, C. Kogel, M. Doyley, J. B. Weaver, and S. P. Poplack, "Magnetic resonance-guided near-infrared tomography of the breast," *Rev. Sci. Instrum.* **75**(12), 5262–5270 (2004).
24. V. Ntziachristos, X. H. Ma, and B. Chance, "Time-correlated single photon counting imager for simultaneous magnetic resonance and near-infrared mammography," *Rev. Sci. Instrum.* **69**(12), 4221–4233 (1998).
25. R. K. Jain, "Normalizing tumor vasculature with anti-angiogenic therapy: a new paradigm for combination therapy," *Nat. Med.* **7**(9), 987–989 (2001).
26. C. H. Schmitz, D. P. Klemer, R. Hardin, M. S. Katz, Y. L. Pei, H. L. Graber, M. B. Levin, R. D. Levina, N. A. Franco, W. B. Solomon, and R. L. Barbour, "Design and implementation of dynamic near-infrared optical tomographic imaging instrumentation for simultaneous dual-breast measurements," *Appl. Opt.* **44**(11), 2140–2153 (2005).
27. S. D. Jiang, B. W. Pogue, A. M. Laughney, C. A. Kogel, and K. D. Paulsen, "Measurement of pressure-displacement kinetics of hemoglobin in normal breast tissue with near-infrared spectral imaging," *Appl. Opt.* **48**(10), 130–136 (2009).
28. S. A. Carp, J. Selb, Q. Fang, R. Moore, D. B. Kopans, E. Rafferty, and D. A. Boas, "Dynamic functional and mechanical response of breast tissue to compression," *Opt. Express* **16**(20), 16064–16078 (2008).
29. C. M. Carpenter, R. Rakow-Penner, S. Jiang, B. L. Daniel, B. W. Pogue, G. H. Glover, and K. D. Paulsen, "Inspired gas-induced vascular change in tumors with magnetic-resonance-guided near-infrared imaging: human breast pilot study," *J. Biomed. Opt.* **15**(3), 036026 (2010).
30. A. Hagen, D. Grosenick, R. Macdonald, H. Rinneberg, S. Burock, P. Warnick, A. Poellinger, and P. M. Schlag, "Late-fluorescence mammography assesses tumor capillary permeability and differentiates malignant from benign lesions," *Opt. Express* **17**(19), 17016–17033 (2009).
31. V. Ntziachristos, A. G. Yodh, M. Schnall, and B. Chance, "Concurrent MRI and diffuse optical tomography of breast after indocyanine green enhancement," *Proc. Natl. Acad. Sci. U.S.A.* **97**(6), 2767–2772 (2000).
32. X. Intes, J. Ripoll, Y. Chen, S. Nioka, A. G. Yodh, and B. Chance, "In vivo continuous-wave optical breast imaging enhanced with indocyanine green," *Med. Phys.* **30**(6), 1039–1047 (2003).
33. S. D. Konecky, G. Y. Panasyuk, K. Lee, V. Markel, A. G. Yodh, and J. C. Schotland, "Imaging complex structures with diffuse light," *Opt. Express* **16**(7), 5048–5060 (2008).
34. J. M. Lasker, J. M. Masciotti, M. Schoenecker, C. H. Schmitz, and A. H. Hielscher, "Digital-signal-processor-based dynamic imaging system for optical tomography," *Rev. Sci. Instrum.* **78**(8), 083706 (2007).
35. B. Michel, L. Novotny, and U. Durig, "Low-temperature compatible IV converter," *Ultramicroscopy* **42**, 1647–1652 (1992).
36. J. M. Masciotti, J. M. Lasker, and A. H. Hiescher, "Digital lock-in detection for discriminating multiple modulation frequencies with high accuracy and computational efficiency," *IEEE Trans. Instrum. Meas.* **57**(1), 182–189 (2008).
37. S. Cova, A. Longoni, and I. Freitas, "Versatile digital lock-in detection technique – application to spectrofluorometry and other fields," *Rev. Sci. Instrum.* **50**(3), 296–301 (1979).
38. P. A. Probst, and B. Collet, "Low-frequency digital lock-in amplifier," *Rev. Sci. Instrum.* **56**(3), 466–470 (1985).
39. S. K. Mitra, *Digital Signal Processing – A Computer Based Approach*, McGraw-Hill, New York, (2001).
40. H. K. Kim, M. L. Flexman, D. J. Yamashiro, J. J. Kandel, and A. H. Hielscher, "PDE-constrained multispectral imaging of tissue chromophores with the equation of radiative transfer," *Biomed. Opt. Express* **1**(4), 812–824 (2010).
41. S. Prahl, "Optical properties spectra," <http://omlc.ogi.edu/spectra/index.html> (2001).
42. A. Corlu, R. Choe, T. Durduran, K. Lee, M. Schweiger, S. R. Arridge, E. M. C. Hillman, and A. G. Yodh, "Diffuse optical tomography with spectral constraints and wavelength optimization," *Appl. Opt.* **44**(11), 2082–2093 (2005).

43. V. R. Stenerud, K. A. Lie, and V. Kippe, "Generalized travel-time inversion on unstructured grids," *J. Pet. Sci. Eng.* **65**(3–4), 175–187 (2009).
44. H. K. Kim and A. H. Hielscher, "A PDE-constrained SQP algorithm for optical tomography based on the frequency-domain equation of radiative transfer," *Inverse Probl.* **25**(1), 015010 (2009).
45. Y. L. Pei, H. L. Graber, and R. L. Barbour, "Influence of systematic errors in reference states on image quality and on stability of derived information for dc optical imaging," *Appl. Opt.* **40**(31), 5755–5769 (2001).
46. F. P. Tiecks, A. M. Lam, B. F. Matta, S. Strebler, C. Douville, and D. W. Newell, "Effects of the valsalva maneuver on cerebral-circulation in healthy adults – a transcranial doppler study," *Stroke* **26**(8), 1386–1392 (1995).
47. L. H. Weimer, "Autonomic testing common techniques and clinical applications," *Neurologist* **16**(4), 215–222 (2010).
48. R. A. Nishimura and A. J. Tajik, "The valsalva maneuver and response revisited," *Mayo Clin. Proc.* **61**(3), 211–217 (1986).
49. M. Suzuki, K. Hori, I. Abe, S. Saito, and H. Sato, "Functional characterization of the microcirculation in tumors," *Cancer Metastasis Rev.* **3**(2), 115–126 (1984).